ORIGINAL PAPER

Exploration of the effect of wing component post-buckling on bending-twist coupling for nonlinear wing twist

Daniel Hahn[1,2] · Matthias Haupt[1,2]

Abstract

A new investigated concept for passive load alleviation is to exploit the nonlinear behavior of wing design components to trigger a deformation which reduce loads once a critical load level is reached. The necessary deformation is a torsional rotation which is supposed to reduce the angle of attack. For this target, wingbox sections are investigated regarding their nonlinear behavior with finite element analysis. Parameter studies feature anisotropic carbon fiber reinforced polymer (CFRP) layups for the skins, layups and thicknesses for spars and the presence of stringers. Results show a desired nonlinear progressive bending-torsion coupling for an unstiffened wingbox section, when the upper skin and the rear spar are modified. After modification they are allowed to buckle within the load envelope. The skin has an anisotropic layup. The rear spar needs to be thinner than the front spar. Both modifications result in progressively increasing torsional rotation of the wingbox with increasing load. Stringers are not applied because they limit the nonlinearity which is not desired for the envisioned load alleviation technique.

Keywords Structural nonlinearity · Structural design · Bending-torsion coupling · Passive load alleviation

1 Introduction

Weight reduction plays a major role in the development of new efficient aircraft. Besides reducing weight by applying materials such as composites with low density and high strength, another possibility is to reduce the load which the structure needs to withstand. Today, airplanes are designed to perform maneuvers with a load factor of 2.5 g. High load levels can also be reached during a gust encounter [33]. For normal operations maneuvers with a load factor of 2.5 g are not needed. If it is made sure via design features, that a load factor of 2.5 g can not occur, the airplane can be designed for a lower load level, which is allowed by certification specification CS 25.337 [12]. This results in a lighter structure.

The limitation of the maximum aerodynamic load which can physically occur is called load control or load alleviation.

There are different approaches to load alleviation. Active load alleviation uses sensors and control surfaces or other actuating measures to adapt the wing to an gust. Basic active load alleviation using the ailerons is already implemented in modern airliners [25] using control surfaces. Research is made on forward looking sensors using LIDARs [14] and advanced actuation such as using piezoelectric actuation in combination with compliant structures to create a smooth morphing wing [17].

Passive load alleviation does not use sensors and actuators. Therefore these components are not needed, which potentially saves weight as well. Additionally it is not prone to system failures, e.g. of electrical nature.

A common approach for passive load alleviation is aeroelastic tailoring. Shirk [27] proposes the definition "Aeroelastic tailoring is the embodiment of directional stiffness into an aircraft structural design to control aeroelastic deformation, static or dynamic, in such a fashion as to affect the aerodynamic and structural performance of that aircraft in a beneficial way." Thus aeroelastic tailoring is not only related to load alleviation like in [22], but can be also used for control effectiveness [32], flutter suppression [6], drag

✉ Daniel Hahn
  daniel.hahn@tu-braunschweig.de

1 Cluster of Excellence SE²A - Sustainable and Energy-Efficient Aviation, Technische Universität Braunschweig, Braunschweig, Germany ,

2 Institute of Aircraft Design and Lightweight Structures, Technische Universität Braunschweig, Hermann-Blenk-Str. 35, D-38108 Braunschweig, Germany

minimization [31], or divergence protection [21]. The directional stiffness in aeroelastic tailoring is mostly based on the anisotropic properties of laminated composite. However, it is also possible, to design structures with isotropic materials and directional stiffness using rib orientation and skin crenelation [1] or a Z-Beam as spar [28]. The tailoring can be uniform for the complete wing like in [20] and [24]. Alternatively, tailoring can be defined individually for divided wing panel sections [8]. Fiber-tow-steering even allows for seamless variation of fiber angles over the wing [29]. Jutte [19] provides a further overview of aeroelastic tailoring studies for transportation aircraft. With increasing aspect ratios, geometric nonlinearity becomes more important and is considered in the aeroelastic analyses [2].

Other approaches for passive load alleviation feature the application of dampers at wing struts, which are able to limit the wing root bending moment in dynamic load events exciting eigenmodes [30]. Another possibility is an unrestrained wingtip attached to a tilted hinge [10].

Recent load alleviation concepts focus on stronger nonlinearities than the rather weak geometric nonlinearity of a beam wing. Strong nonlinearity in this context refers to buckling of e.g. composite shells [13]. Also the postbuckling behavior of composite shells [7] provides interesting nonlinear features. Dong [11] used the buckling and postbuckling behavior with a mode change to create a dampening element. Imperfections influence the buckling behavior of composite shells [18]. In dynamic compression loads with frequencies higher than the first eigenfrequency of a cylindrical composite shell, the dynamic buckling load are increased compared to the static critical loads [35]. Another strong nonlinearity is mode jumping in the post buckling regime, as shown for thermomechanical loading of composite plates [3].

Load alleviation approaches exploiting strong nonlinear features improve the hinged wingtip from [10] with a nonlinear negative stiffness spring device [9]. Arrieta [4] replaces a beam in a compliant airfoil by a bistable composite strip, which snaps sharply into its second stable state at a critical compression load. This second stable state has lower stiffness in compression direction and the airfoil changes its camber to alleviate load. The bistable strip does not snap back into its original state without actuation. Runkel [26] works on quadratic box beam structures that exhibit bend twist coupling due to instabilities in a single web, which are used as wing spars.

The authors' project within the cluster of excellence SE²A (Sustainable and Energy-Efficient Aviation) investigates on this approach for passive load alleviation which aims to exploit nonlinear behavior of the wing design components to trigger significantly increased deformation above a critical load level. Such nonlinear behavior can be the postbuckling behavior of a part. The stiffness of the part changes in the postbuckling regime. This change affects the stiffness distribution of the whole wing and thus the deformation. The deformation is supposed to be tailored to shapes which reduce lift. Such deformations are downward twist and camber line or profile changes, like in classical aeroelastic tailoring. The difference to classical aeroelastic tailoring is the aim for significant nonlinear behavior, which keeps the deformation small below the critical load, but increases the deformation disproportionately high above the critical load.

The first project phase focuses on the basic understanding of the design of wing components with specified significant nonlinear behavior. This paper explores possibilities to design wing components with nonlinear progressive bending-torsion coupling. The selected component is a simplified section of the wingbox between two ribs, which is modified to show nonlinearity. According to the concept this wingbox segment is supposed to exhibit progressive bending-torsion coupling. This deformation leads to reduced loads in the wing part outboard of the modified segment. The postbuckling behavior is tailored using anisotropic fiber reinforced polymer laminates. At this stage the target is the structural nonlinear behavior under load. The aeroelastic interaction with fluid and therefor changing loads and the response is not yet covered. Also material failure is not covered, since the focus is how to design the structural nonlinear behavior using postbuckling behavior of anisotropic materials, not the material itself.

The basic idea of exploiting nonlinearities for progressive load alleviation is similar to Runkel [26] and Arrieta [4]. In contrast to Runkel [26], who worked with quadratic box beams used as single spar, the dimensions of the wingbox in the authors' research are designed to represent a single aisle transport aircraft. Furthermore the laminate layups are not unidirectional and the influence of the layering sequence is investigated. Also instabilities in the skin and pressure forces on the skin are covered. Bistable laminates gaining their instability from internal stresses due to the thermal curing of the asymmetric laminate like in Arrieta [4] are not used in the authors' approach. Instead, focus is set on elastic buckling, which resumes to the original state, when the structure is unloaded.

Sect. 2 describes the methods and baseline configuration. The parametric studies are presented and discussed in Sect. 3. Sect. 4 concludes the paper.

2 Methods

This research uses finite element analysis with the commercial toolbox *Abaqus* to analyze the structural behavior of a simplified wingbox section.

Table 1 wingbox section dimensions

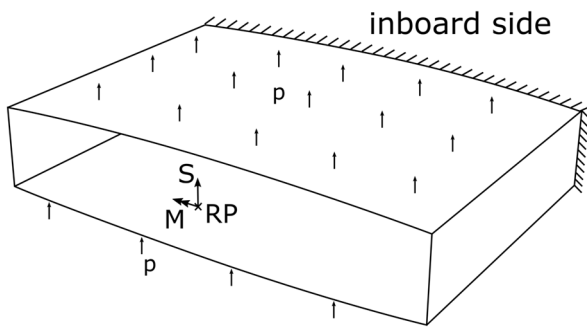|	
Distance between ribs	400 mm
Distance between spars	585 mm
Radius of circular arc	3.4 m
Skin thickness	4 mm
Spar thickness	4 mm
Spar height	105 mm

Fig. 1 Sketch of the wingbox section model. *S* shear, *M* bending moment, *RP* reference point, *P* pressure

2.1 Reference configuration

In the research cluster SE^{2}A three aircraft reference configurations are developed. These consist of a short range, medium range and long range aircraft, each being platform of new and for the mission appropriate technologies [23]. The load alleviation concept of this paper is based on the medium range configuration. The first version of the medium range configuration has a high aspect ratio backward swept wing. This wing is the basis for the derivation of a simplified geometry for the structural models. These simplifications are done to produce more generic results. The loads are estimated using weight information from the reference configuration.

2.2 Wingbox model

The models represents a wingbox section in the area between the spars and two ribs in the outer wing, at 17 m of 19.33 m half span. To generate more general results the profile is approximated by a circular arc and tapering and sweep are neglected. The dimensions are given in Table 1 and the model is depicted in Fig. 1. The skin thickness is selected to buckle within the load envelope.

The material is generic carbon fiber reinforced polymer (CFRP) with 57 % fiber volume fraction and epoxy matrix. The material parameters for an unidirectional layer are taken from the material database of *eLamX*^{2} [15] and given in Table 2. The listed material parameters are Young's

Table 2 Material parameters of an unidirectional layer

$E_\parallel$	129 GPa
$E_\perp$	7.38 GPa
$\nu_{\parallel\perp}$	0.319
$G_{\parallel\perp}$	4.48 GPa
ϱ	1560 kg·m^{-3}

Table 3 Load magnitudes

M	24.5 kNm
S	26.5 kN
p	84.51 kPa

modulus parallel and perpendicular to fiber direction $E_\parallel$ and $E_\perp$, Poisson's number $\nu_{\parallel\perp}$, shear modulus $G_{\parallel\perp}$ and density ϱ. The baseline layup is a quasi isotropic aircraft design laminate with a $[45/-45/90/0]_s$ layup. The fractions of these layers for the skin are (0.2, 0.2, 0.15, 0.45). The same stacking sequence is used for the spars, however, the layers are equally distributed. Material failure is not taken into account.

The wingbox is clamped at the inboard rib and constrained as rigid body on the outboard rib. The reference point for the rigid body is located in the center of the outboard rib. Since both ribs are defined by constraints they are not modeled as solid. At the reference point of the outboard rib shear force *S* and bending moment *M* are applied. Beginning with the cases discussed in Sect. 3.3 there are additional pressure loads *p* acting on the panels. The maximum loads are modeled with a basic Shear Moment Torsion (SMT) approach, assuming an elliptical lift distribution. The total lift at 2.5 g equals the reference configurations maximum take off weight force of 530.25 kN with factor 2.5. Counteracting weight of the wing and engine structure are taken into account for calculation of the wing internal loads. The loads are scaled linearly with respect to the 2.5 g model case. Load magnitudes at 2.5 g are given in Table 3. No torsional moment is applied as external load, which would be present in a real wing. However, this is a decision for the study design with the idea, that all observed rotations stem from induced moments rather than external applied loads. The pressure is calculated by distributing the local line load *q* modeling the elliptical lift distribution onto the surface. 0.33 of the pressure is applied on the lower skin, 0.67 of it is applied on the upper skin with a negative sign to represent suction on the skin.

The load history features a static step to 1 g, followed by a *1-cosine*-gust shape load to 2.5 g as maximum in an implicit dynamic step. Since 1 g represents the stationary flight state and no snap-through behavior is supposed to happen until 1 g using a static step is the most efficient. The gust load is calculated in the time domain. This allows to capture snap-through
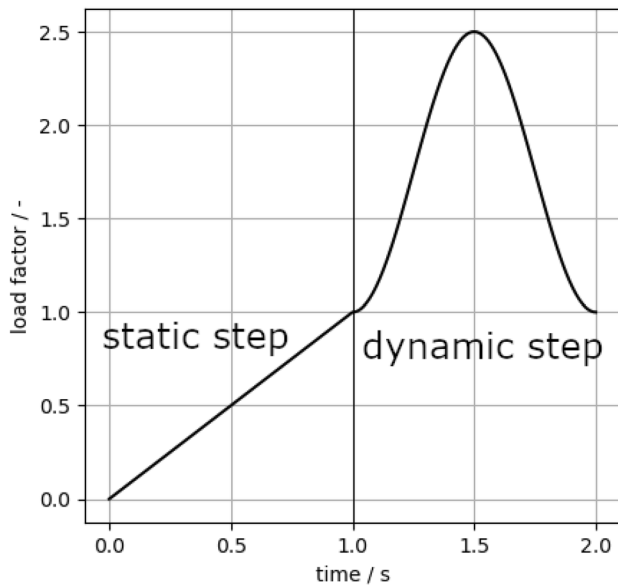
Fig. 2 load history

Fig. 3 convergence study

induced oscillations. The implicit scheme using Newton's method is more time efficient than the explicit scheme, because the step size in implicit calculations is orders of magnitudes larger than in the explicit scheme for most parts of the calculation. In the baseline case the gust duration is 1 s, which represents a gust length of 214 m at an airspeed of 214 ms^{-1} based on the ranges given in certification specification CS25.341 [12]. The load history is depicted in Fig. 2.

Results of interest for this model are the maximum translational displacement u_{max} and rotational displacement φ_{max} for the free section and the gradients in the respective load-displacement curves $\delta n/\delta u$, respectively $\delta n/\delta \varphi$, with load factor n. The ratio of the gradients at 0 g and 2.5 g is an indicator for the structural nonlinearity, where a value of 1 represents linearity. The ratios are defined as translational stiffness ratio

$$R_t = \frac{\delta n}{\delta u}(n = 2.5\text{g})/\frac{\delta n}{\delta u}(n = 0\text{g}) \tag{1}$$

and rotational stiffness ratio

$$R_r = \frac{\delta n}{\delta \varphi}(n = 2.5\text{g})/\frac{\delta n}{\delta \varphi}(n = 0\text{g}). \tag{2}$$

Field displacements are also considered to evaluate buckling modes. The model uses 5.000 linear quadrilateral shell elements with reduced integration and hourglass control. The selected mesh size is based on the convergence study depicted in Fig. 3 with the baseline model. The mesh is visible in Fig. 9, which is a later figure showing results. 9.
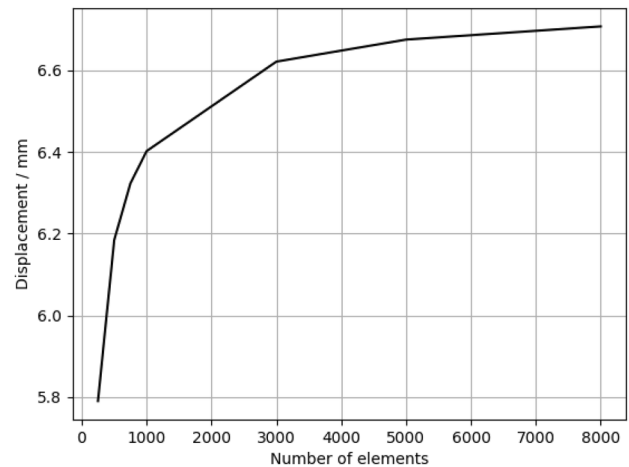
2.3 Variations of parameters

Parametric studies are conducted to gain basic understanding of their influence on the nonlinear behavior in the post-buckling regime. The target behavior is progressive bending-torsion coupling, as further elaborated in Sect. 3.1. Variations of the following parameters are analyzed:

skin:

– Ply rotation angles for different layers in different skins
– Layer stacking sequence

spar:

– Thickness
– Crossply orientation
– Balanced ply laminate angle and orientation

stringer:

– Number of stringers

conditions:

– Aerodynamic pressure

Since the target of this paper is a basic understanding, no optimization methods are used. In later stages optimization methods could be considered, which is challenging in a highly nonlinear regime with possible unstable snap-through behavior.

3 Simulation results

In this section results of the parametric studies are shown, analyzed and discussed with regard to the application for load alleviation.

3.1 Desired behavior

For the evaluation of the results it is necessary to define an aimed behavior. In backward swept wings, upward bending is beneficial for load alleviation and avoiding torsion divergence. The reason is the reduction of the effective angle of attack because of the geometry. For a forward swept wing, upward bending is not beneficial. The same geometric effects lead to an increased angle of attack and thus increased load. This behavior is described by Wright [34]. Forward swept wings are currently in the interest of research because of their advantages regarding laminar flow [5]. A second possibility to reduce the angle of attack is the rotation of the wingbox which leads to a twisting of the wing. This kind of deformation is beneficial for load alleviation independently of wing sweep. For this reason focus and priority of this research is given to the rotational motion compared to upward bending. Since the wing is mainly loaded by a bending moment, the desired behavior is a bending-torsion coupling.

The aim of this project is to design a nonlinear load alleviation, such that the structure does not deform much below a critical load level. At higher loads it is supposed to deform disproportionately high with load. So it is not the aim to reach the largest possible rotational deformation, if this results in a structure which rotates linear with load. Within this paper a nonlinear behavior with large differences between the rotational stiffness at 0g and at 2.5g is desired. A significant rotation is still necessary, but not the only target.

3.2 Skin ply layup rotations

In the first series of models the ply layup of the skin panels is modified. The basic idea is like aeroelastic tailoring but extended into the postbuckling regime. Selected plies are rotated by an angle α from their initial direction. α covers the range from 0° to 45° within each series of models. At 45° rotation a ply reaches the direction of another ply from the baseline laminate. Several cases with different layer selections for rotation are investigated to explore the different effects. There are cases where layers in in both skins are selected for rotation, but also cases where just the upper skin is modified. Either the complete layup or just the 0° layers are rotated in the different models. In case the layers are rotated in both skins, both the same direction and alternating

Table 4 Case numbering

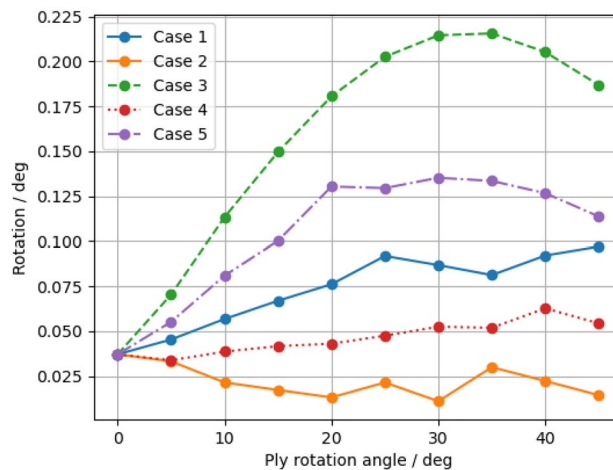|	Upper skin	Lower skin
Case 1	$[45+\alpha/-45+\alpha/90+\alpha/\alpha]_s$	$[45+\alpha/-45+\alpha/90+\alpha/\alpha]_s$
Case 2	$[45+\alpha/-45+\alpha/90+\alpha/\alpha]_s$	$[45-\alpha/-45-\alpha/90-\alpha/-\alpha]_s$
Case 3	$[45/-45/90/\alpha]_s$	$[45/-45/90/\alpha]_s$
Case 4	$[45+\alpha/-45+\alpha/90+\alpha/\alpha]_s$	$[45/-45/90/0]_s$
Case 5	$[45/-45/90/\alpha]_s$	$[45/-45/90/0]_s$

Fig. 4 Maximum rotation of the wingbox. For the case legend refer to Table 4

directions are tested. A legend with case numbering and specific layups for the subsequent discussion is given in Table 4. This first model series does not include the pressure load.

The resulting maximum rotations for these variations are depicted in Fig. 4. Without ply rotation the cases show a torsional rotation of 0.0325° at maximum load. This is due to different distances of the plies in 45° direction to the middle surface, which result in an asymmetric case in the post buckling regime. Case 3 has the highest maximum rotation, when the layers are rotated by 35°. The second highest value is reached by case 5. Like in case 3 not all plies are rotated. The cases 1,2 and 4, where all plies are rotated together show less torsional rotations. This difference can be explained by the different anisotropic material behaviors. According to classical lamination theory (CLT), if the whole layup is rotated, the stiffness distribution is also rotated, but the maximum and minimum values stay the same. If only one ply is rotated, the total stiffness values are redistributed for the orientations, because the direction difference between neighboring plies changes. This results in higher maximum and lower minimum values and thus higher anisotropic behavior. The difference is shown with polar plots of the orientation dependent stiffness values of the layup with 35° rotation in Fig. 5. The plots are calculated with the
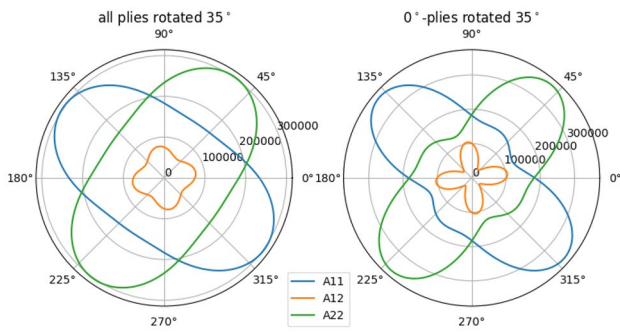
Fig. 5 Polar plots of stiffness values for different layups

tool *eLamX*^{2} [15]. A_{11}, A_{12} and A_{22} measure longitudinal, transverse and shear stiffness of the layup and are entries in the ABD-Matrix. In such polar plots isotropic materials are represented by circles. Anisotropic behavior is visible by the deviation of the visible shape from circles. The shape of the layup with only the 0°-layer rotated is slimmer than the layup with all plies rotated. Applied in the wingbox skin this higher anisotropy leads to larger rotations. In case 2, the rotation in alternating directions leads to a small decrease in maximum rotation.

Figure 6 shows the rotation behavior of case 5 with 35° ply rotation in the time domain during loading and unloading between 1 g and 2.5 g. After a smooth initial rise the structure starts to oscillate. This oscillation is excited by a snap-through buckling of the upper skin. The parameters of interest are not evaluated from the plots in the time domain. Instead, load-displacement and load-rotation curves are used. Since the calculation is still from the time domain, the oscillations are still visible in such curves, even if they
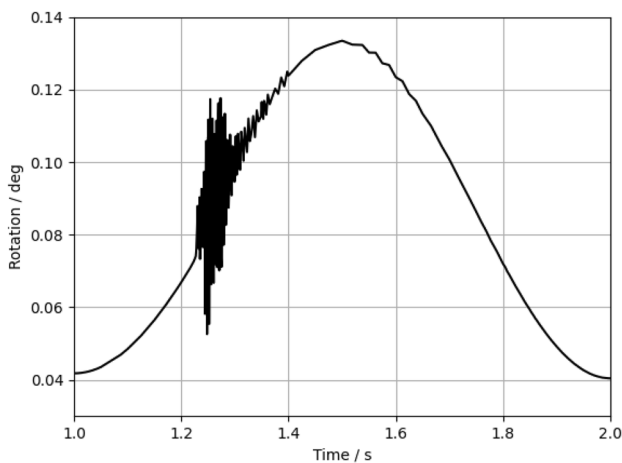
are basically time independent. If the loading was applied slower, the oscillations would cover a smaller band in the load factor range. The load-rotation curves for all cases with a ply rotation angle of 35° are depicted in Fig. 7. All curves show the oscillations beginning between 1.5 g and 1.7 g, when the skin starts to buckle with a snap-through. The resulting buckling buckling mode is also depicted in Fig. 7. Due to the anisotropy the bulges from buckling are not symmetrical but skewed. The sudden pulse from snap-through excites eigenmodes. The gradients before and after the snap-throughs differ from each other, most visible for cases 1 and 5.

Analogous to stiffness, which is measured by the gradient of a load-displacement curve, the term rotational stiffness refers to the gradients of the load-rotation curve. Since there is no rotational external force, this term may be misunderstood. It refers not directly to the stiffness against a rotational force, but to the rotation induced by the applied load combination. The ratio between the rotational stiffness at 0 g and 2.5 g are depicted in Fig. 8. The cases differ between declining and progressive stiffness behavior. Progressive behavior has a rotational stiffness ratio over 1 and means, that the wingbox rotates more before buckling than in the postbuckling regime during the loading process. Declining behavior with a ratio below 1 on the other hand means that it rotates more after the nonlinearity. Declining stiffness behavior corresponds to progressive bending-torsion coupling and is the desired behavior. Thus the best suiting behavior out of this series is found in case 5 with a ply rotation angle of 35°, because of its still significant maximum rotation and desired
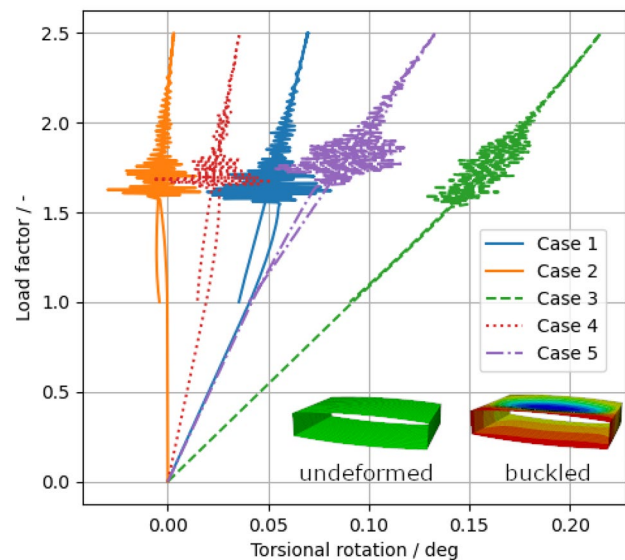

Fig. 6 Time-rotation curves for case 5 with ply rotation of 35 deg. and 1 s gust duration

Fig. 7 Load-rotation curves for a ply rotation of 35 deg and 1 s gust duration. For the case legend refer to Table 4
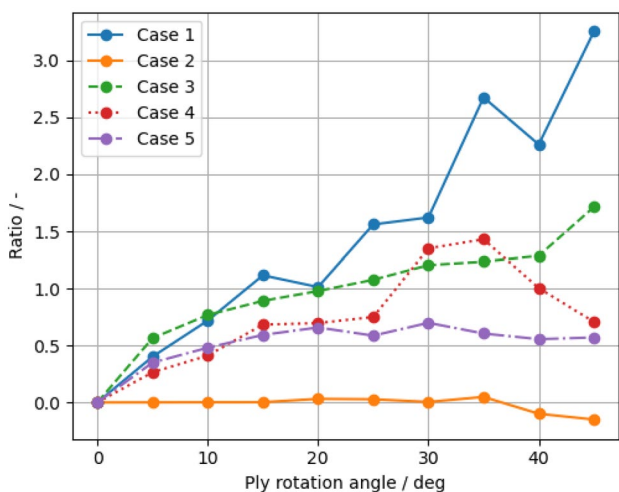
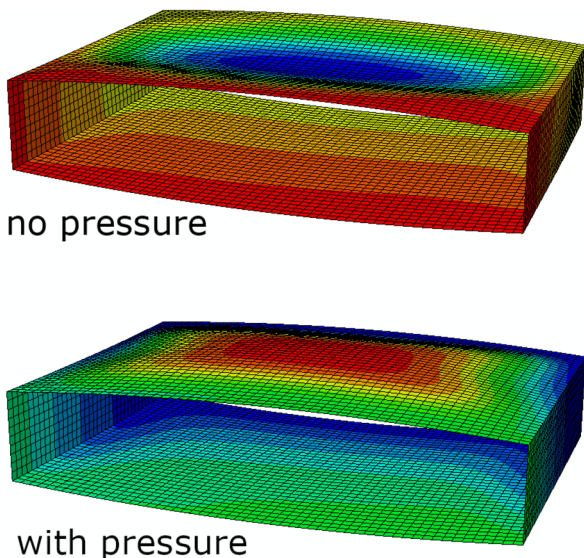**Fig. 8** Ratio of the rotational stiffnesses. For the case legend refer to Table 4

Fig. 9 Buckling shape with and without pressure load

declining rotational stiffness ratio. Cases 1, 2 and 4 are not further investigated due to their low torsional rotation.

3.3 Influence of aerodynamic pressure

The cases in Sect. 3.2 only consider bending and shear force. To get more realistic load conditions, a pressure force is added. This addition changes the buckling behavior. Without pressure load, the skin bulges to the inside of the wingbox. With pressure, the skin bulges to the outside of the wingbox. These two different shapes are shown in Fig. 9. The dynamics of the two modes also differ from each other. The

buckling mode to the inside buckles with a snap-through behavior. This means a sudden instability. The mode with pressure does not have such a sudden change in the shape. Due to the evolving pressure load, the skin is deformed from the beginning, which acts like an imperfection. This results in a smoother behavior. This difference can be seen well in the curves of the translational displacement in Fig. 10. It has to be noted, that Fig. 10 looks like the stiffness of the case with pressure was lower because of its lower slope. However, the reason for the lower slope is not reduced stiffness. Instead the overall load is higher, because the pressure component is added to the other load components. The snap-through is visible by the horizontal line with subsequent oscillations. This oscillations come from the pulse-like change, which excites many frequencies including the eigenfrequencies of the structure. The shown data is from case 5 (Table 4) with a rotation value of 35°. This basic behavior is also observed for case 3.

As visible in Fig. 10 the translational stiffness ratio is higher in the case with pressure. A series of models based on case 3 applies pressure values between 0 and 150 % of the initially modeled pressure as given in Table 3. It shows, that the critical pressure fraction, at which the change between the modes takes place, is between 50 % and 55 % pressure. It can be seen by the sharp rise in the stiffness ratios in Fig. 11. This percentage is only valid for the load distribution at the particular position on the wing. At other wing positions, the load is distributed in different ratios among the load components bending, shear and pressure.
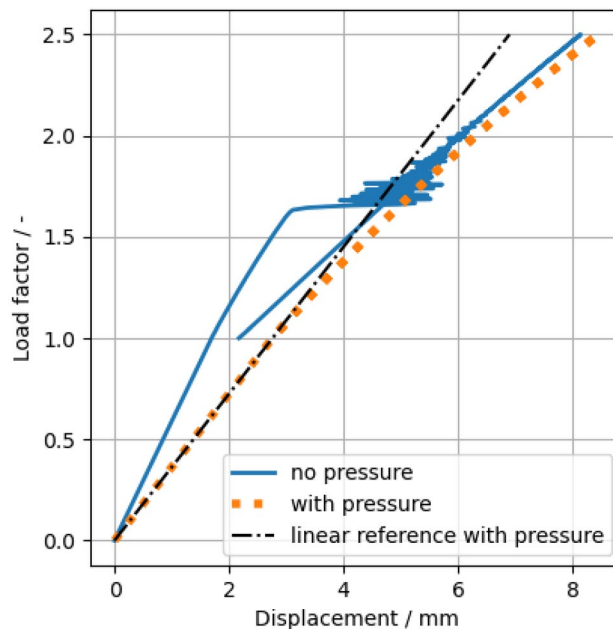

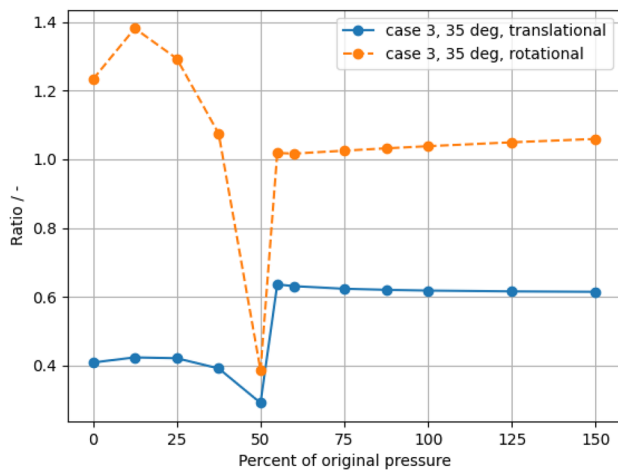**Fig. 10** Load-displacement curve showing snap-through and soft nonlinear behavior

Fig. 11 Stiffness ratios with different pressure load fractions

As visible in Fig. 11, the rotational stiffness is also affected. In case 3 the maximum rotational stiffness ratio decreases from 1.7 to 1.1, when pressure is applied. In case 5 on the other hand the maximum rotational stiffness increases from 0.7 to 1.45 with applied pressure. These values are the maximum values from all considered ply rotation angles. The different buckling shapes have different postbuckling stiffnesses resulting in different stiffness distributions in the whole wingbox, which is a reason for the differences in the rotational stiffness ratios.

3.4 Ply stacking sequence

As stated in Sect. 3.2 the distance to the middle surface of plies which are not aligned along the skin panel edges influence the asymmetric postbuckling shape. This also holds true for the thick, rotated former 0°-layers. This effect is only present, if the layers are thick and have therefor a unique lever arm. If the layup is build out of many thin plies in sequential order, this effect is expected to become less significant, because the anisotropic effects of each layer are smeared over the complete range of possible distances. For the wingboxes in case 3 and 5 (Table 4) with a ply rotation value of 35°, the 35°-layer is in the center of the symmetric layup. For these two cases two additional models are used, in which the 35°-layers are shifted to the outside of the symmetric laminates. All four models include aerodynamic pressure. The changes on the maximum rotation and the rotational stiffness ratio are given in Table 5. It shows that increasing the influence of the rotated layers by shifting them to the outside of the layup results in declining stiffness ratios even though aerodynamic pressure is applied. The stacking sequence thus is a possibility to mitigate the undesired increase of the stiffness ratio as consequence of the imperfection, which is introduced by the pressure.

Table 5 Results for different ply stacking sequences for max. rotation φ_{max} and rotational stiffness ratio R_r

Case, 35°-layers	φ_{max} / deg	R_r / -
Case 3, centered	0.24	1.04
Case 3, outside	0.14	0.71
Case 5, centered	0.13	1.09
Case 5, outside	0.11	0.65

3.5 Spar ply layup

Not only the skins can have nonlinear behavior, but also the spars. To get buckling in the spars, they need to be thinner than they are in the baseline model. To get a downward rotation of the wingbox segment the rear spar is thinner than the front spar. This is based on the assumption that reduced spar stiffness leads to stronger upward motion at the respective spar. The new baseline model for spar alterations has spar thicknesses of 2 mm for the front and 1.5 mm for the rear spar. With the baseline skin thickness of 4 mm and weakened spars the wingbox shows unstable snap-through buckling before reaching 2.5 g because of the reduced spar stiffness. Increasing the skin thickness to 5.5 mm results in a structure with stable nonlinear behavior until 2.5 g. The dimensions for the model used for spar modification analyses are given in Table 6.

Different rear spar layups are modeled. The layups each have two ply directions with equally distributed ply thicknesses. The first type of layup is a crossply layup. In crossply layups, the plies are orientated perpendicular to each other. The front spar layup is $[45/-45]_s$ because of the stiffness against expected shear in the spar. The rear spar layups are varied. With a $[0/90]_s$ layup as baseline case this crossply is rotated in the range from -40° to 45° in 5° steps. Extending the range would lead to redundant results since every possible orientation of the crossply is covered within one quarter circle. This spar modification is modeled for two cases with different skin modification. The first series has the skin from the baseline case. The second series combines the spar modification with a skin modification. For the skin modification case 3 with 35° rotation is used.

Table 6 dimensions of the wingbox section for spar modifications

Distance between ribs	400 mm
Distance between spars	585 mm
Radius of circular arc	3.4 m
Skin thickness	5.5 mm
Front spar thickness	2 mm
Rear spar thickness	1.5 mm
Spar height	105 mm

Figure 12 shows the maximum rotation for both cases. Both curves show the same shape with a nearly constant difference. This shows, that the effect of the skin modification is combined with the effect of the spar modification regarding the maximum rotation. The highest maximum rotation is achieved with the $[0/90]_s$ orientation. The lowest rotation is found at the $[40/-50]_s$ orientation. Since spars are shear loaded and $[45/-45]_s$ layups provide high stiffness against shear loads these results support the assumption that lower stiffness in the rear spar leads to larger rotation. The rotational stiffness ratios in Fig. 13 have similar results. The highest values are obtained for the $[0/90]_s$ layup. With this layup the rotational stiffness ratio is at 0.9 without skin modification and 1.05 with skin modification. In both cases the rotational stiffness ratio decreases towards $[45/-45]_s$ layups. At $[45/-45]_s$ are the lowest values of 0.1 without and 0.55 with skin modification. The ratios are high for the layups with high rotation. This is because the high rotation is not primarily triggered by buckling. Instead the rotation already starts at low loads because the lower stiffness at the rear spar is present also in the pre buckling phase. A corresponding load-rotation curve is a nearly linear line.

The second layup type is a balanced ply laminate. This means that for each ply with positive angle θ there is a ply with the same thickness and angle $-\theta$. The layup can be rotated by an angle α leading to the layup structure $[\alpha + \theta / \alpha - \theta]_s$. Two model series varying the rotation angle θ are analyzed. The two series differ in the layup rotation α. α is $0°$ in the first and $45°$ in the second series. In both series the rotation angle θ is in the range between $0°$ and $90°$ in $10°$ steps. The skin is modified with case 3 and $35°$ rotation angle.
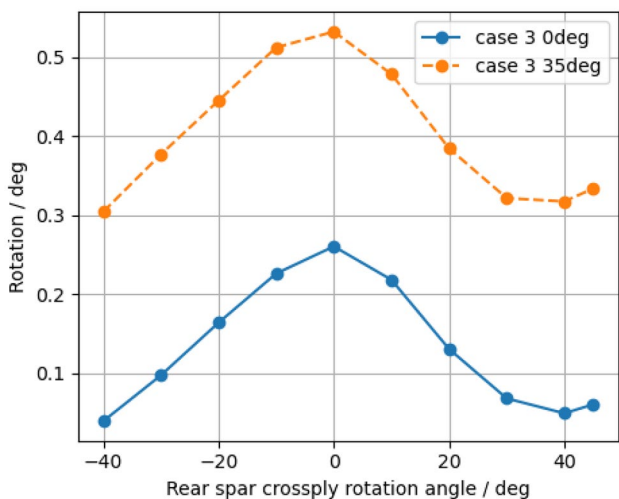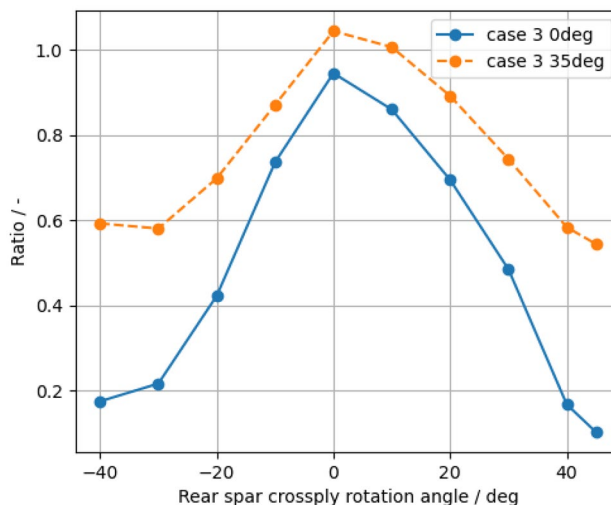

Fig. 13 Rotational stiffness ratio for rotated rear spar crossplies with and without skin modification

The results for maximum torsional rotation are shown in Fig. 14. The maximum value of $0.57°$ is achieved with the unidirectional $[0]$ layup. The lowest value of $0.32°$ is reached by a $[60/-60]_s$ layup. The span of values is smaller for the rotated reference orientation. The minimum value of $0.395°$ is found with a $[25/65]_s$ layup, the maximum value of $0.52°$ with a $[95/-5]_s$ layup.

Fig. 15 shows the rotational stiffness ratios for the balanced ply laminates. Like for the crossplies there is a tendency, that for large rotations large stiffness ratios are obtained. However, they are slightly different. For the $[45]_s$ and $[55/35]_s$ layup the maximum rotation is higher than in the $[25/65]_s$ layup, which is not represented in the rotational stiffness ratio. The rotational stiffness ratio is lower for these
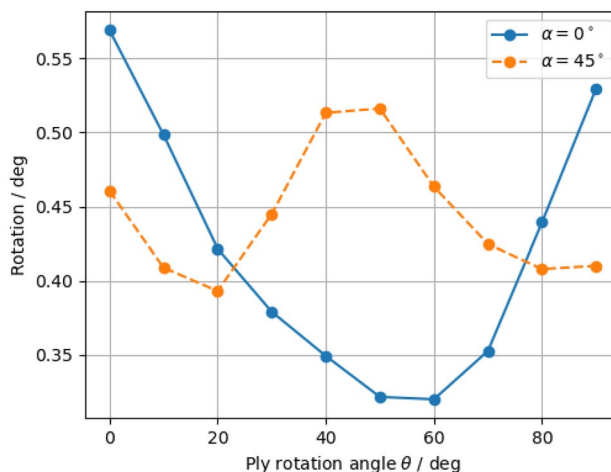

Fig. 12 Maximum rotation for rotated rear spar crossplies with and without skin modification

Fig. 14 Maximum rotation with different angles for a balanced ply layup in the rear spar
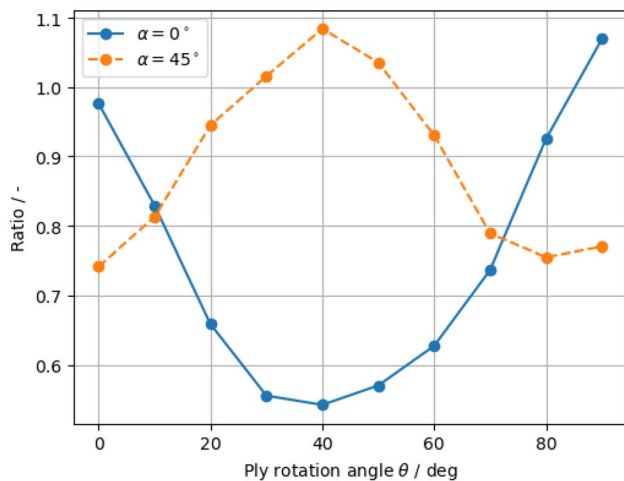
Fig. 15 Rotational stiffness ratio with different angles for a balanced ply layup in the rear spar

Table 7 skin ply sequence cases

L1	$[45/-45/90/0]_s$
L2	$[90/0/-45/45]_s$
L3	$[0/90/45/-45]_s$

two cases. Another difference are the minimums for the layups with $\alpha = 0°$. The rotation minimum is at $[60/-60]_s$, while the minimal rotational stiffness ratio is at $[40/-40]_s$. Therefor, $[40/-40]_s$ is a layup that matches the desired behavior. In general, for the proposed load alleviation concept the rear spar should be weaker than the front spar and allowed to buckle. But if the difference is large, a large amount of the rotation is independent from the nonlinearity.

3.6 Layup variations including spar modification

Getting closer to the desired behavior the ply sequence and layup cases are further investigated with a model now including the spar modifications. The selected spar layup is $[40/-40]_s$ in the rear spar. *mod. Case 3* and *mod. Case 5* are introduced, in which not only the former 0°-ply, but also the former 90°-ply is rotated. The skin rotation angle is 35°. Different ply orders are modeled and summarized in Table 7 in their initial form before ply rotation.

Table 8 shows maximum rotation φ_{max} and rotational stiffness ratio R_r for different combinations. The lowest R_r is in mod. Case 5 with layup L3, which is an upper skin with rotated 0°-ply and rotated 90°-ply, with the 0°-ply at the outside. In this model the maximum rotation is the highest of Case 5 variations. Case 3 and the according variations have higher maximum rotations and higher rotational stiffness ratios. The desired behavior is best met by *mod. Case*

Table 8 Results for max. rotation φ_{max} and rotational stiffness ratio R_r with modified layups

Case, ply sequence	φ_{max} / deg	R_r / -
Case 3, L1	0.35	0.54
mod. Case 3, L1	0.31	0.55
mod. Case 3, L2	0.42	0.38
Case 5, L1	0.22	0.42
mod. Case 5, L1	0.23	0.37
mod. Case 5, L2	0.23	0.36
mod. Case 5, L3	0.30	0.27

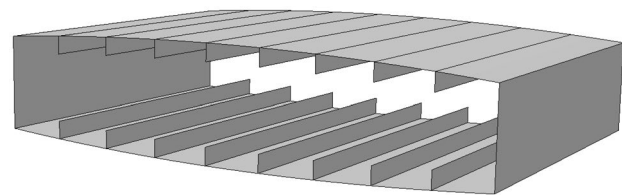**Fig. 16** Wingbox segment with 8 stringers per skin

5, L3 because of its low rotational stiffness ratio and still comparably high rotation values.

3.7 Influence of basic stringers

The deformed wingbox segments do not only show torsional rotational but also significant bending. Significant bending is not part of the desired behavior. The application of simple linear stringers is modeled to investigate if bending can be reduced while maintaining the torsional rotation. The stringers are 20 mm high and 2 mm thick. This is rather small for the reason to still allow nonlinearity. They are distributed equally on the skin panels. The stringer layup is a $[45/-45]_s$ layup. The wingbox design is *Case 3, L1*, but with a slightly thinner skin of 3.5 mm for all models. The spar thicknesses are 2 mm and 1.5 mm, but the layup differs slightly from Sect. 3.5 because the model is based on an older version of the baseline selections. The front spar has an equally distributed $[45/-45/0/90]_s$ layup. The rear spar has the same sequence but the 0° and 90° layers together are 80% of the layup. The idea behind this layup was the high rotation of the $[0/90]_s$ crossply layup with a bit of added stability in other directions. But this did not consider the rotational stiffness ratio. A model with 8 stringers per skin is depicted in Fig. 16.

Figure 17 shows the relative translational and rotational maximum displacements when stringers are added. It is visible that translational displacements are more restrained by the stringers than rotational displacements. This matches the expectations since stringers are supposed to strengthen the
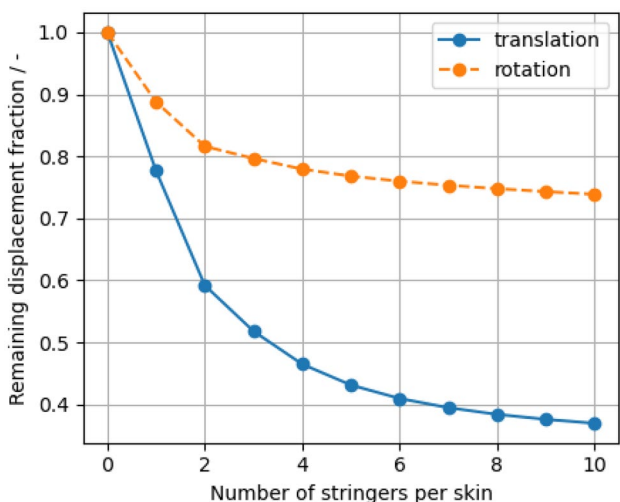
Fig. 17 Remaining relative maximum displacement with stringers

bending stiffness. This different effect on the translations favors stringers for the investigated load alleviation concept. Unfortunately there are significant drawbacks in terms of the rotational stiffness ratio as seen in Fig. 18. The rotational stiffness ratio increases significantly when stringers are added. The reason for that is the added resistance against buckling which lowers the magnitude of the geometric non-linearity. Because of the significantly increased rotational stiffness ratio, simple linear stringers are not considered beneficial for the desired behavior in this configuration. More studies regarding simple stringers varying stringer size and skin thicknesses have been done but are not discussed further in this paper since they do not provide advantages for the desired behavior either. Models with unconventional stringer concepts like differently spaced or rotated stringers are planned.
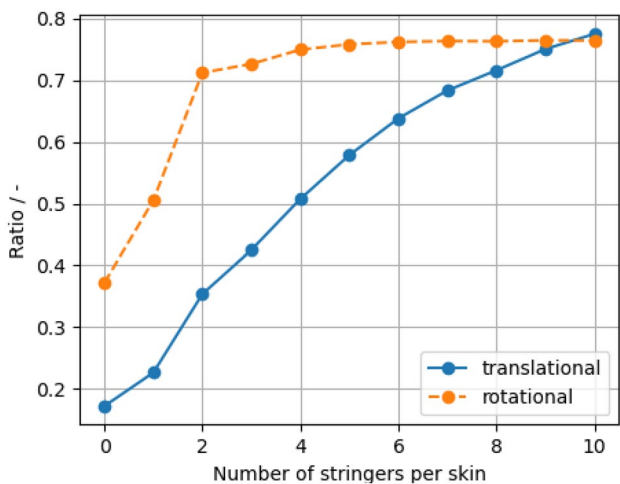

Fig. 18 Stiffness ratios with stringers

3.8 Influence of the boundary conditions

The model of the wingbox segment is directly fixed at the inboard rib and the outboard rib is a rigid body. These boundary conditions are stiffer than a wing structure. To assess the influence of the boundary conditions on the behavior of the modified wingbox segment, the *mod. Case 5, L3* model is extended by one conventional rib bay on both sides. These rib bays have no rotated plies and spars without reduced thickness. Six stringers with 30 mm height and 5 mm thickness are added on both skins in the attached rib bays. Two ribs with 6 mm thickness are included between the three segments. The shear and bending moment, which now are located further away from the wing box segment of interest are reduced such that the forces at the boundary between to the wingbox segment of interest and the loaded rib bay remain the same. To accommodate for the increasing bending moment towards the clamped side, the skin thickness in the clamped rib bay is increased from 5.5 mm to 6 mm. The extended model and a corresponding deformation plot is depicted in Fig. 19.

Figure 20 shows the load-displacement and load-rotation curves for the extended model and the directly fixed model. The displacement and rotation in the extended model describe the motion of the outboard rib with respect to the inboard rib including all translational and rotational degrees of freedom. The results show a difference between the models, but the general behavior remains comparable.

The difference depends on the stiffness of the rest of the wing. In a stiffer design the difference becomes smaller and in a weaker design it becomes larger. When a wing is
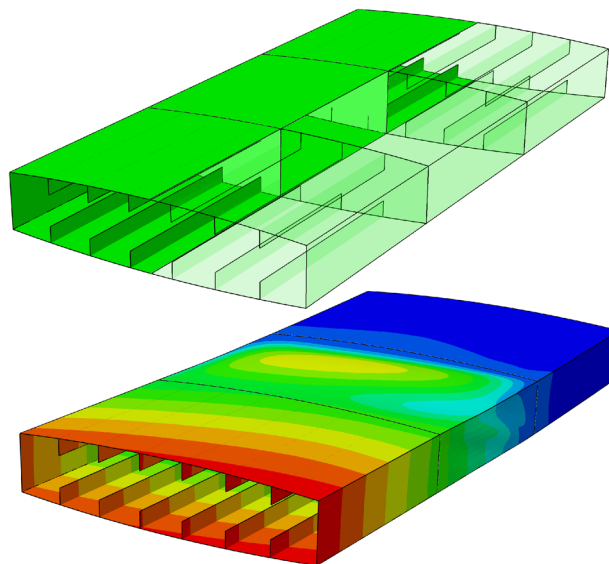

Fig. 19 Undeformed and deformed contour of the extended model with attached rib bays
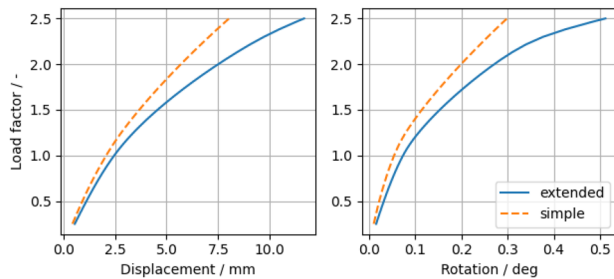
Fig. 20 Load-displacement and load-rotation curves of the modified wingbox with attached rib bays (extended) and with directly fixed boundary conditions (simple)

designed to include a modified wingbox segment, this has to be taken into account in the sizing.

This paper focuses on the influence of design choices on the tailored segment, so the stiff boundary condition can be used for this purpose. The results provide guidelines on how to modify a wingbox segment for nonlinear bending-torsion coupling.

3.9 Differences between spanwise positions

Up to this point the wingbox models featured only one position at the wing span in the outer wing. At different positions the balance between the different load components changes. According to the load model (Sect. 2.2) shifting towards the inside of the wing the elliptical lift line load flattens out. The pressure load is calculated using this line load. The shear force increases approximately linear and the bending moment increases approximately quadratic. So at wing positions nearer to the wing root the bending moment tends to dominate more over pressure and shear force than in the outer wing.

Additionally to the different ratios of load magnitudes, the wingbox aspect ratio also changes, if the rib distance is considered equal over the whole span. These influences have not been studied in detail. Considering the influence of the pressure load on stiffness ratios, the stiffness ratio could be more suited for the proposed load alleviation at positions shifted towards the wing root, where the pressure influence is reduced compared to the bending moment.

These theses motivate the sizing and simulation of a wingbox segment nearer to the wing root to explore, if there is potential to improve the desired behavior. Its span wise position is set to 13 m, which is shifted towards the wing root compared to 17 m from the former series of models. Table 9 shows the adjusted load magnitudes.

To allow for significant torsional rotation, the wingbox segment length should not be too small in comparison with the spar distance. Therefor one rib in the middle of the segment is removed. The wingbox segment thus has the length

Table 9 Load magnitudes

M	356.2 kNm
S	138.4 kN
p	46.12 kPa

Table 10 wingbox section dimensions

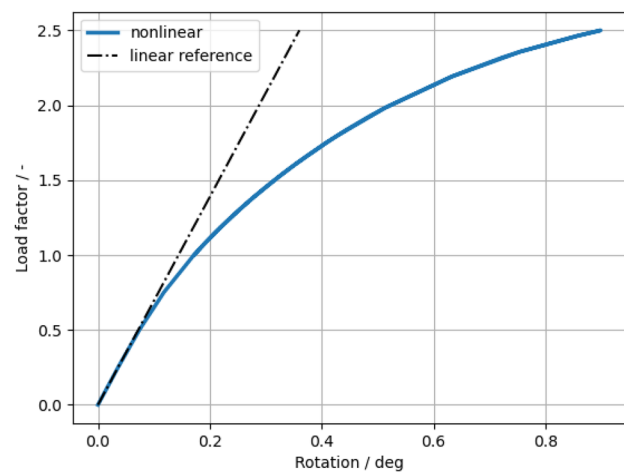|	
Distance between ribs	800 mm
Distance between spars	850 mm
Radius of circular arc	5.5 m
Skin thickness	13 mm
Front spar thickness	6 mm
Rear spar thickness	4 mm
Spar height	180 mm

Fig. 21 Load-rotation curve of the tailored wingbox

of two initial rib distances. The spar and skin thicknesses are sized to have the desired behavior in the load range to 2.5 g. The dimensions are given in Table 10.

The skin layup corresponds to *mod. Case 5, L3* with a ply rotation of 35° for the initial 0° and 90° plies in the upper skin. The 35° ply is located at the outside of the layup. The front spar has a $[45/-45]_s$ layup. The rear spar has a lower thickness (Table 10) than the front spar and a $[40/-40]_s$ layup. The wingbox section is not stiffened by stringers.

The resulting load-rotation curve is depicted in Fig. 21. The desired declining stiffness behavior is visible by the declining gradient of the curve. A linear behavior with the same initial gradient is visualized by the reference line. The distance between the reference line and the blue line corresponds to the increased rotation by the nonlinearity. The maximum rotation is 0.9° and the rotational stiffness ratio 0.17.

This rotation is higher than the achieved rotation with the small wingbox in the outer wing. This supports the theses, which motivated the analyses of this model. The progressively increasing rotation is considered suited for the investigated load alleviation concept.

Another difference when implementing the modified wingbox closer to the wing root are effects with the larger remaining outer wing structure. A rotation of a segment nearer to the wing root affects more of the wing. On the other hand the reaction speed of the wing deformation could be slower due to the outer wing's inertia.

3.10 Discussion of limitations

This study focuses on design choice influences for the tailoring of components with structural nonlinearities for load alleviation. There are several challenges to face before it can be applied in a real system. The first challenge is material failure. This aspect has not been studied in this research. Due to comparably large displacements for a CFRP material, failure could occur. It could be necessary to refine the geometry design at key points or change the material to a more flexible material with comparable anisotropic properties.

Overall the structure is less stiff in this segment. This decreases flutter speed and torsional divergence speed. Torsional divergence is especially important for forward swept wings.

The model only represents the wingbox segment itself. As discussed in Sect. 3.8, when such a tailored wingbox segment is included into a full wing, the sizing of the wingbox and of the rest of the wing influence each other and need to be considered together. The missing outer wing string structure affects the dynamic simulations resulting in faster reaction because there is no inertia from the outer wing structure and fuel mass. The load case has been simplified compared to a real wing as well. This is particular the case for the pressure load distribution, which is uniform over the whole skin surface. Inertia and pressure distribution effects will be accounted for in fluid structure simulations.

In a real wing a torsional moment is present. For the application of this concept, this has to be considered in the sizing process.

4 Conclusions and outlook

This paper discussed fundamental research on structures for a new load alleviation concept exploiting the nonlinear structural behavior of wing design components. It is shown by the simulations that a wingbox section with progressive nonlinear bending-torsion coupling can be designed using nonlinearities of the components. Material failure is not taken into account at this stage and will be considered in

the future. Both upper skin and rear spar are designed to buckle within the load envelope. The upper skin uses an anisotropic CFRP ply layup, $[35/-55/45/-45]_s$ with ply fractions (0.45, 0.15, 0.2, 0.2.). The rear spar is thinner than the front spar and uses a slightly adapted layup of $[40/-40]_s$ instead of $[45/-45]_s$ as in the front spar. Both measures lead to the progressive nonlinear bending-torsion coupling which is considered to be beneficial for passive load alleviation.

The differences in span wise position are only covered briefly with one case. In following studies this aspect will be investigated in more detail, such that the concept can be applied in the most valuable position.

The behavior with more realistic aerodynamic loads of wings including this modified wingbox section will be evaluated in upcoming investigations which will couple structure and fluid simulations using the in-house coupling environment *ifls* [16]. This will allow to assess the effectiveness of the proposed wing box segment for load alleviation and the assessment of the weight reduction of the wing.

Declarations

Conflict of interest The authors declare that they have no conflict of interest.

References

1. Abdelkader, A., Harmin, M., Cooper, J., Bron, F.: Aeroelastic tailoring of metallic wing structures. In: 52nd AIAA/ASME/ASCE/AHS/ASC structures, structural dynamics and materials conference. American Institute of Aeronautics and Astronautics, Reston, Virigina (2011). https://doi.org/10.2514/6.2011-1712

2. Afonso, F., Vale, J., Oliveira, É., Lau, F., Suleman, A.: A review on non-linear aeroelasticity of high aspect-ratio wings. Prog. Aerosp. Sci. **89**, 40–57 (2017). https://doi.org/10.1016/j.paerosci.2016.12.004

3. Álvarez, J.G., Bisagni, C.: Investigation on buckling and mode jumping of composite plates under thermomechanical loads. Int. J. Non-Linear Mech. **138**, 103837 (2022). https://doi.org/10.1016/j.ijnonlinmec.2021.103837

4. Arrieta, A.F., Kuder, I.K., Rist, M., Waeber, T., Ermanni, P.: Passive load alleviation aerofoil concept with variable stiffness multistable composites. Compos. Struct. **116**, 235–242 (2014). https://doi.org/10.1016/j.compstruct.2014.05.016

5. Beck, N., Landa, T., Seitz, A., Boermans, L., Liu, Y., Radespiel, R.: Drag reduction by laminar flow control. Energies **11**(1), 252 (2018). https://doi.org/10.3390/en11010252

6. Bendiksen, O.O.: Recent developments in flutter suppression techniques for turbomachinery rotors. J. Propuls. Power **4**(2), 164–171 (1988). https://doi.org/10.2514/3.51283

7. Bisagni, C.: Numerical analysis and experimental correlation of composite shell buckling and post-buckling. Compos. Part B: Eng. **31**(8), 655–667 (2000). https://doi.org/10.1016/S1359-8368(00)00031-7

8. Bordogna, M.T., Lancelot, P., Bettebghor, D., de Breuker, R.: Static and dynamic aeroelastic tailoring with composite blending and manoeuvre load alleviation. Struct. Multidiscip. Optim. **61**(5), 2193–2216 (2020). https://doi.org/10.1007/s00158-019-02446-w

9. Castrichini, A., Cooper, J.E., Wilson, T., Carrella, A., Lemmens, Y.: Nonlinear negative stiffness wing-tip spring device for gust loads alleviation. In: 15th Dynamics Specialists Conference, p. 1701. American Institute of Aeronautics and Astronautics, Reston, Virginia (2016). https://doi.org/10.2514/6.2016-1574

10. Castrichini, A., Hodigere Siddaramaiah, V., Calderon, D., Cooper, J.E., Wilson, T., Lemmens, Y.: Nonlinear folding wing-tips for gust loads alleviation. In: 56th AIAA/ASCE/AHS/ASC Structures, Structural Dynamics, and Materials Conference, p. 4. American Institute of Aeronautics and Astronautics, Reston, Virginia (2015). https://doi.org/10.2514/6.2015-1846

11. Dong, L., Lakes, R.S.: Advanced damper with negative structural stiffness elements. Smart Mater. Struct. **21**(7), 075026 (2012). https://doi.org/10.1088/0964-1726/21/7/075026

12. EASA: Certification Specifcations CS25 Amendment 17. https://www.easa.europa.eu/sites/default/files/dfu/CS-25 Accessed 04.12.2020

13. Ferreira, A.J.M., Barbosa, J.T.: Buckling behaviour of composite shells. Compos. Struct. **50**(1), 93–98 (2000). https://doi.org/10.1016/S0263-8223(00)00090-8

14. Fezans, N., Joos, H.D.: Combined feedback and LIDAR-based feedforward active load alleviation. In: AIAA Atmospheric Flight Mechanics Conference. American Institute of Aeronautics and Astronautics, Reston, Virginia (2017). https://doi.org/10.2514/6.2017-3548

15. Hauffe, A.: eLamX^2. https://tu-dresden.de/ing/maschinenwesen/ilr/lft/elamx2/elamx. Accessed 26.08.2020

16. Haupt, M., Nies, R., Unger, R., Horst, P.: Computational aero-structural coupling for hypersonic applications. In: 9th AIAA/ASME Joint Thermophysics and Heat Transfer Conference, p. 3252 (2006)

17. Henry, A.C., Molinari, G., Rivas-Padilla, J.R., Arrieta, A.F.: Smart morphing wing: optimization of distributed piezoelectric actuation. J. Intell. Mater. Syst. Struct. **57**(6), 2384–2393 (2019). https://doi.org/10.2514/1.J057254

18. Hilburger, M.W., Starnes, J.H.: Effects of imperfections of the buckling response of composite shells. Thin-Walled Struct. **42**(3), 369–397 (2004). https://doi.org/10.1016/j.tws.2003.09.001

19. Jutte, C.V., Stanford, B.K.: Aeroelastic tailoring of transport aircraft wings: state-of-the-art and potential enabling technologies (2014). https://ntrs.nasa.gov/api/citations/20140006404/downloads/20140006404.pdf. Accessed 20.09.2021

20. Kameyama, M., Fukunaga, H.: Optimum design of composite plate wings for aeroelastic characteristics using lamination parameters. Comput. & Struct. **85**(3–4), 213–224 (2007). https://doi.org/10.1016/j.compstruc.2006.08.051

21. Krone, N.J.: Divergence elimination with advanced composites. In: Aircraft Systems and Technology Meeting. American Institute of Aeronautics and Astronautics, Reston, Viriginia (1975). https://doi.org/10.2514/6.1975-1009

22. Krüger, W.R., Dillinger, J., de Breuker, R., Haydn, K.: Investigations of passive wing technologies for load reduction. CEAS Aeronaut. J. **10**(4), 977–993 (2019). https://doi.org/10.1007/s13272-019-00393-2

23. Liu, Y., Elham, A., Horst, P., Hepperle, M.: Exploring vehicle level benefits of revolutionary technology progress via aircraft design and optimization. Energies **11**(1), 166 (2018). https://doi.org/10.3390/en11010166

24. Qin, Z., Marzocca, P., Librescu, L.: Aeroelastic instability and response of advanced aircraft wings at subsonic flight speeds. Aerosp. Sci. Technol. **6**(3), 195–208 (2002). https://doi.org/10.1016/S1270-9638(02)01158-6

25. Regan, C.D., Jutte, C.V.: Survey of applications of active control technology for gust alleviation and new challenges for lighter-weight aircraft (2012). https://ntrs.nasa.gov/archive/nasa/casi.ntrs.nasa.gov/20120013450.pdf. Accessed 03.08.2020

26. Runkel, F., Fasel, U., Molinari, G., Arrieta, A.F., Ermanni, P.: Wing twisting by elastic instability: a purely passive approach. Compos. Struct. **206**, 750–761 (2018). https://doi.org/10.1016/j.compstruct.2018.07.095

27. Shirk, M.H., Hertz, T.J., Weisshaar, T.A.: Aeroelastic tailoring—theory, practice, and promise. J. Aircraft **23**(1), 6–18 (1986). https://doi.org/10.2514/3.45260

28. Stodieck, O.: Tech-insight: aeroelastic tailoring of wings using a Z-beam concept (2019)

29. Stodieck, O., Cooper, J.E., Weaver, P.M., Kealy, P.: Improved aeroelastic tailoring using tow-steered composites. Compos. Struct. **106**, 703–715 (2013). https://doi.org/10.1016/j.compstruct.2013.07.023

30. Szczyglowski, C.P., Neild, S.A., Titurus, B., Jiang, J.Z., Cooper, J.E., Coetzee, E.: Passive gust loads alleviation in a truss-braced wing using integrated dampers. In: International Forum on Aeroelasticity and Structural Dynamics, IFASD (2017)

31. Thuwis, G.A.A., de Breuker, R., Abdalla, M.M., Gürdal, Z.: Aeroelastic tailoring using lamination parameters. Struct. Multidiscip. Optim. **41**(4), 637–646 (2010). https://doi.org/10.1007/s00158-009-0437-6

32. Weisshaar, T., Nam, C., Batista-Rodriguez, A.: Aeroelastic tailoring for improved UAV performance. In: 39th AIAA/ASME/ASCE/AHS/ASC Structures, Structural Dynamics, and Materials Conference and Exhibit. American Institute of Aeronautics and Astronautics, Reston, Viriginia (1998). https://doi.org/10.2514/6.1998-1757

33. Wingrove, R.C., Bach, R.E.: Severe turbulence and maneuvering from airline flight records. J. Aircraft **31**(4), 753–760 (1994). https://doi.org/10.2514/3.46557

34. Wright, J.R., Cooper, J.E.: Introduction to aircraft aeroelasticity and loads. AIAA education series. Wiley, Chichester (2008)

35. Zaczynska, M., Abramovich, H., Bisagni, C.: Parametric studies on the dynamic buckling phenomenon of a composite cylindrical shell under impulsive axial compression. J. Sound Vib. **482**, 115462 (2020). https://doi.org/10.1016/j.jsv.2020.115462